

Article

Structural Characterisation of Zeolites Derived from Lithium Extraction: Insights into Channel- and Cage-Type Frameworks

Leonardo Leandro dos Santos ¹, Rubens Maribondo do Nascimento ² and Sibele Berenice Castellã Pergher ^{1,*} ¹ Laboratory of Molecular Sieves, Department of Chemistry, Federal University of Rio Grande do Norte, Natal 59078-970, Brazil; leo.leandro25@gmail.com² Postgraduate Program in Materials Science and Engineering, Federal University of Rio Grande do Norte, Natal 59078-970, Brazil; rmaribondo@ufrnet.br

* Correspondence: siblepergher@gmail.com

Abstract: This study investigates the structural and adsorption characteristics of channel- and cage-type zeolites obtained through lithium extraction. Through XRD, FT-IR spectroscopy, and adsorption isotherm analyses, distinct adsorption behaviours of CH₄ and CO₂ were observed in both zeolite types. Cage-type zeolites exhibited higher adsorption capacities attributed to their structural advantages, highlighting the importance of structural framework selection in determining adsorbent efficacy. The presence of structural defects and an amorphous phase influenced adsorption behaviours, while thermodynamic data underscored the role of adsorbate properties. Kinetics studies revealed the influence of the structural framework on CH₄ adsorption and CO₂ adsorption kinetics. Analysis of adsorbate–adsorbent interactions demonstrated robust interactions, particularly with LPM16-Y. These findings offer insights into the potential applications of zeolites in gas adsorption processes, emphasising the importance of structural properties and adsorbate characteristics in determining adsorption performance.

Keywords: lithium extraction by-product; cage-type zeolite; channel-type zeolite; CH₄/CO₂ competitive adsorption



Citation: Santos, L.L.d.; Nascimento, R.M.d.; Pergher, S.B.C. Structural Characterisation of Zeolites Derived from Lithium Extraction: Insights into Channel- and Cage-Type Frameworks. *Minerals* **2024**, *14*, 526. <https://doi.org/10.3390/min14050526>

Academic Editor: Natale Perchiazzi

Received: 2 April 2024

Revised: 6 May 2024

Accepted: 16 May 2024

Published: 20 May 2024



Copyright: © 2024 by the authors. Licensee MDPI, Basel, Switzerland. This article is an open access article distributed under the terms and conditions of the Creative Commons Attribution (CC BY) license (<https://creativecommons.org/licenses/by/4.0/>).

1. Introduction

The extraction of lithium from beta-spodumene involves a series of chemical processes, including acid leaching, calcination, and solubilisation with chemical additives containing actinides, resulting in the production of Li₂CO₃ and a silica-aluminous residue. Chen and co-workers recently outlined various methods for lithium extraction from beta-spodumene, yielding Si- and Al-rich aluminosilicate residue alongside residual lithium in exchangeable ion form. They proposed utilising this aluminosilicate residue post-extraction for synthesising molecular sieves, specifically zeolites [1].

Zeolites are well known for their microporous structures and serve as efficient adsorbents across multiple industries, aiding in the separation of gases such as CH₄, NH₃, H₂S, N₂, O₂, and CO₂ [2]. Despite extensive research on microporous zeolites of FAU and MOR topology, the understanding of the interplay between the structure, adsorption characteristics, and physicochemical properties of these materials remains incomplete, especially concerning gas adsorption at ambient or slightly elevated temperatures [3].

Gas adsorption studies are essential for comprehending processes like gas separation, purification, and storage. Factors such as Si/Al ratio, crystallinity, pore size, and surface area, alongside adsorbate properties, influence gas adsorption characteristics [4–6]. Therefore, elucidating the relationship between different zeolite structures, including channel- and cage-like configurations, and diverse adsorbents is critical.

This study presents the synthesis of zeolites of FAU and MOR topologies through a modified lithium extraction procedure, where lithium salt and zeolite are recovered as the primary product and by-product, respectively. Subsequently, a comprehensive

structural characterisation of these materials is conducted to provide insights into channel and cage-type structures.

2. Materials and Methods

Beta-spodumene, provided by Companhia Brasileira de Lítio (CBL), with a Si/Al molar ratio of 2.6, was utilised. Its chemical composition is detailed in Table 1. Reagents utilised include aluminium hydroxide (99+%, Dinâmica) (Dinâmica, São Paulo, Brazil), ammonium bicarbonate (99+%, Synth) (Synth Chemical, Bologna, Italy), demineralised water, Aerosil 200 fumed silica (99.8%, Sigma) (Sigma-Aldrich, St. Louis, MO, USA), sodium carbonate (99.5%, Dinâmica), and sodium hydroxide (98+%, Sigma).

Table 1. Chemical analysis of the beta-spodumene sample (wt%).

Component	SiO ₂	Al ₂ O ₃	Li ₂ O	Fe ₂ O ₃	K ₂ O	Others
Content (%)	68.97	22.31	6.43	0.92	0.42	<0.40

The experimental process is outlined in Figure 1. A strategic approach was devised for lithium recovery while promoting a by-product with zeolite characteristics: to produce a by-product akin to FAU zeolite, the procedure commenced with the reflux digestion of approximately 1.0 g of ground beta-spodumene in 50 mL of 0.75 mol/L NaOH solution at 80 °C for around 4 h. The resulting paste was mixed with a solution containing about 3.0 g of Al(OH)₃ to adjust the final Si/Al ratio (SAR) (or any alternative source of aluminium to adjust the SAR of the desired zeolite from the initial beta-spodumene) along with 1.0 g of Na₂CO₃ dissolved in 50 mL of 2.0 mol/L NaOH solution and left under moderate agitation for 30 min. The resulting gel, with an approximate molar composition of 10Na₂O:1Al₂O₃:5or11SiO₂:170H₂O:0.2Li₂O, was then subjected to treatment in a Teflon-lined autoclave at 90 °C for 6 h under static conditions. To facilitate the recovery of lithium salt during the leaching phase, ammonium salt was added to the supernatant at room temperature, followed by filtration, gentle stirring, and overnight drying at 60 °C to precipitate Li₂CO₃ crystals from the filtrate and recover zeolitic solids from the slurry retained on the filter paper; the cooled autoclaved solution underwent solubilisation with approximately 3.5 g of NH₄HCO₃ at room temperature for 4 h. The solution was then filtered and washed until the supernatant reached a pH < 8, followed by overnight drying in an oven to obtain a zeolite by-product resembling zeolite X (designated LPM16-X) and similar to zeolite Y (LPM16-Y) when approximately 1.8 g of Al(OH)₃ was used in stage 2. Similarly, to produce a by-product with the characteristics of mordenite zeolite, the procedure utilised approximately 1.0 g of ground beta-spodumene refluxed in 50 mL of 1.2 mol/L NaOH solution. Subsequently, around 21.4 g of aerosil silica was added to the autoclaved gel with a molar composition of 6Na₂O:1Al₂O₃:30SiO₂:765H₂O:0.2Li₂O, followed by exposure to 150 °C for 48 h in a Teflon autoclave. After treatment with NH₄HCO₃, filtration, and oven drying, the resulting by-product comprised a MOR-type zeolite (LPM17). In general, lithium recovery rates were achieved through recirculation of the mother liquor from the filtered lithium bicarbonate solutions, yielding a lithium content of 290 mg/L without further enrichment.

The structural properties of the zeolites were characterised using XRD (PANalytical CUBIX, X'Celerator) (Malvern Panalytical, Worcestershire, UK), SEM (JEOL, JSM 6300 model with Link-Isis) (JEOL Ltd., Tokyo, Japan), and FT-IR (Nicolet 710 FT-IR Spectrometer) (Thermo Fisher Scientific, Waltham, MA, USA) to aid in understanding their adsorption and gas-zeolite interaction characteristics. The intensities of specific diffraction peaks in the sample were compared to those of a commercial standard sample to calculate relative crystallinity (the synthesised zeolites were compared with commercially available NaX, NaY, and mordenite). The SAR data of our faujasite and mordenite samples were inferred from the unit cell parameter obtained in XRD patterns and a combination of techniques primarily involving intensity ratios of the characteristic peaks in XRD patterns

and subsequently confirmed through energy dispersive X-ray spectroscopy (EDS elemental analysis) of samples recovered in stage 4 [7]. Specifically, peak intensities corresponding to the mordenite structure were employed for this calculation, ensuring that the estimate was specific to our synthesised mordenite phase. Physicochemical properties of the microporous solids, such as specific surface area, micropore volume, mesopore and macropore volume, pore size, and distribution, were determined from N_2 adsorption data using a Micromeritics Model TriStar 3000 (Micromeritics Instrument Corporation, Norcross, GA, USA) and the BET equation. Surface area (BET method) and average pore diameters for the zeolite samples (BJH adsorption) were calculated using the ASAP 2020 physisorption analyser's software (Version 2.00). Each zeolite underwent vacuum pretreatment at 673 K for 2 h to remove water and other sorbed materials. The solid samples were then weighed in a sample tube, cooled to 77 K (liquid nitrogen temperature), and exposed to nitrogen gas at low pressure (gradually increasing to 1 bar) to measure the volume of gas adsorbed at equilibrium (cm^3/g) against the partial pressure of the adsorbate (p/p_o). Gas adsorption characteristics were analysed using methane (CH_4) and carbon dioxide (CO_2) as adsorbates, with measurements including capacity (gravimetric method using thermal gravimetric analyser—PerkinElmer, TGA) (PerkinElmer, Waltham, MA, USA), rate, and isotherms of gas adsorption at 298 K, assessing gas–solid interactions by measuring the amount of adsorbed gas in mol per gram of solid adsorbent (mmol/g).

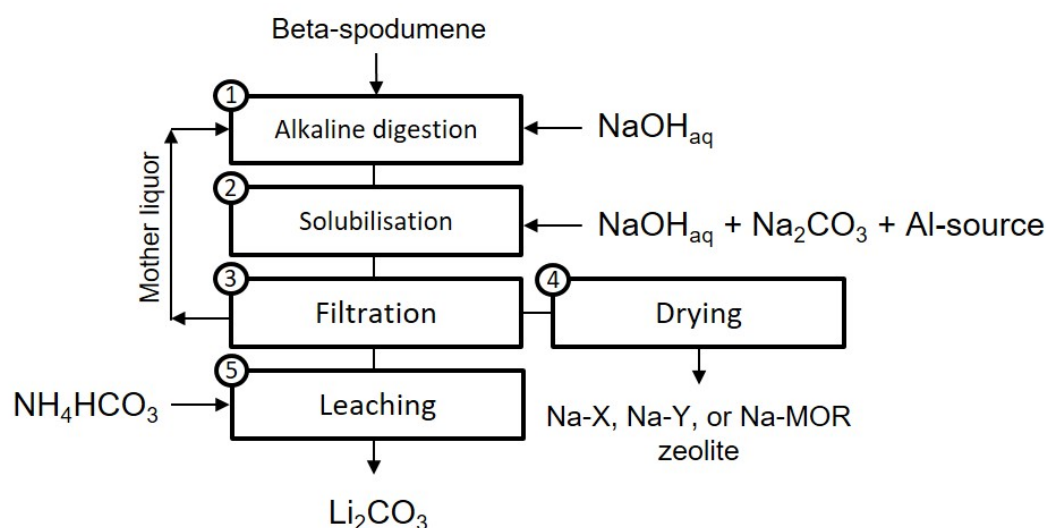


Figure 1. Flowchart of the experimental procedures used in this study.

3. Results and Discussion

3.1. Structural Framework

The structural framework of each material recovered in stage 4 after drying was assessed by comparing the XRD patterns of the samples with simulated patterns [8], shown in Figure 2. The XRD patterns of materials LPM16-X and LPM16-Y resemble faujasite topology (hence only one XRD pattern is shown). Materials LPM16-X and -Y differ in terms of SAR, with LPM16-X having a SAR of 2.4 and LPM16-Y a SAR of 5.0, both in the sodium form. In contrast, the patterns of material LPM-17 resembled the topology of sodium mordenite, showing a SAR of approximately 18 [9], significantly higher than that predicted by the gel composition.

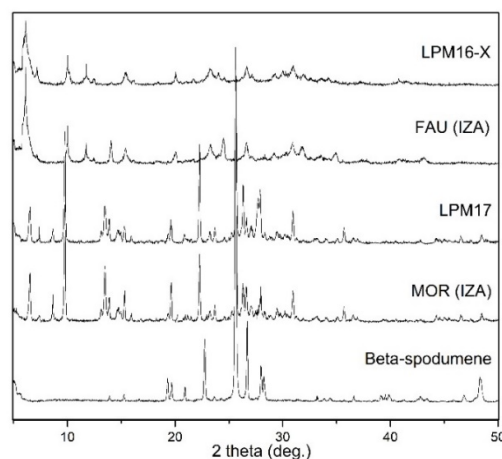


Figure 2. XRD patterns of the by-products resulting from the process illustrated in Figure 1.

The IR spectra of the zeolite by-products in the $1400\text{--}400\text{ cm}^{-1}$ region underwent analysis (see Figure S1 and Table S1 Supplementary Materials).

Two classes of characteristic vibrations were identified: internal vibrations, insensitive to structural variations, and vibrations linked to external connections between tetrahedra, sensitive to the structural framework [8]. The stretching band at $950\text{--}1250\text{ cm}^{-1}$, which is SAR-sensitive, shifts to a lower frequency with increasing Al content. This information is depicted in Supplementary Figure S1, where the highest wavenumber elongation modes are assigned to SAR = 13.6 (1097 cm^{-1}) and SAR = 4.5 (1035 cm^{-1}) for LPM16-Y and LPM16-X, respectively [10]. Additionally, a double ring presence in the $540\text{--}585\text{ cm}^{-1}$ region, independent of SAR, was observed [11]. Other bands associated with the structure's topology, attributed to external binding modes, appeared near $1050\text{--}1150\text{ cm}^{-1}$ in the asymmetric stretching region [10].

The XRD patterns, FT-IR spectra, and morphology (Supplementary Figure S2) aided in classifying the obtained materials into two groups: (i) cage-type zeolites (LPM16-X and LPM16-Y), possessing an internal pore system of interconnected cavities, and (ii) a channel-type zeolite (LPM17), characterised by a two-dimensional channel system.

3.2. Physicochemical Properties

In the Supplementary Materials (Figure S3), the N_2 adsorption isotherms of cage- and channel-type zeolites are presented. The experimental isotherm for the channel-type zeolite (LPM17) exhibits a type I isotherm with a slight slope at the end, indicating the presence of a mesoporous or external area [5]. Conversely, the adsorption isotherms for the cage-type zeolites demonstrate a rapid increase in adsorbed amount followed by a plateau at higher pressures, indicative of a limited volume of the adsorbed phase due to microporosity [12]. Additional data on the area of micropores, volume, and mean pore diameter are provided in Table 2. The results suggest structural differences between the zeolite types, which influence their adsorption behaviour.

The calculated area encompasses both micropore and outer-surface areas, providing space for gas molecule adsorption. This confirms a larger surface area for cage-type zeolites, consistent with data reported by Zeolyst International for FAU ($760\text{--}885\text{ m}^2/\text{g}$) [12]. This variance can be attributed to the complexity of surface area access, influenced by pore blockage, resulting in the lower nitrogen adsorption observed in channel-type zeolites [5]. The one-dimensional pore network of mordenite structures presents more pore blockages than the open three-dimensional structural configurations found in faujasites [13]. Consequently, faujasites offer advantages in terms of surface area and pore volume, facilitating greater adsorbent accumulation and absorption within the cage structure.

Table 2. Adsorption isotherm data, micropore area, volume, and mean pore diameter.

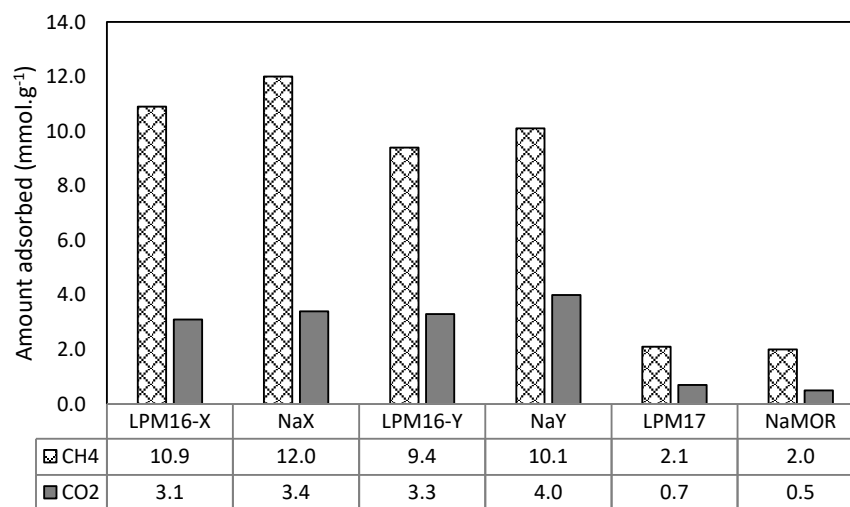
By-Product	RC ¹ (%)	Surface Area (m ² /g)		Pore Volume (cm ³ /g)		APD ² (nm)
		BET	Micropore	Micropore	Meso/Macro	
LPM16-X	79	552.4	539.5	0.20	0.022	1.48
LPM16-Y	83	833.1	808.6	0.29	0.026	1.58
LPM17	100	505.1	452.9	0.17	0.070	2.96

¹ Relative crystallinity; ² average pore diameter.

Additionally, these structures exhibit relatively smaller mean pore diameters compared to channel-type zeolites, attributed to faujasites' ability to maintain microporosity [8]. The larger pore diameter observed in channel-type zeolites arises from the presence of meso- and macropores, contributing to the total pore volume. The average pore size accounts for both micropore and meso–macropore dimensions [12].

3.3. Gas Adsorption Capacity

The assessment of CH₄ and CO₂ adsorption capacity on cage- and channel-type zeolites at 323 K and 1 bar was conducted (Figure 3). The results indicate that cage-type zeolites exhibit superior adsorption capacity compared to channel-type zeolites, with a consistent trend observed across LPM16-X > LPM16-Y > LPM17 for CH₄ and LPM16-Y > LPM16-X > LPM17 for CO₂. Though no explicit factors justify the variation in adsorption capacity between the gases, CH₄ shows relatively higher adsorption than CO₂, possibly due to the structural and physicochemical properties of the adsorbents elucidated in this study.

**Figure 3.** CH₄ and CO₂ adsorption capacity in channel- and cage-type zeolite by-products.

Equally important to adsorption capacity is the total accessible volume. The FAU topology boasts one of the largest accessible volumes among framework structures (27.4% of the IZA database), more than double that of the MOR topology (12.27%). While this information directly explains the variance in gas adsorption capacity between LPM16 and LPM17 zeolites, we will maintain a focus on distinguishing between channel and cage structures throughout the text.

Cage-type structures outperform channel-type structures, likely due to the presence of supercage and sodalite cages that encapsulate adsorbents within the structure [14]. However, the interconnected pore network between channels and cages can influence adsorbate diffusivity, where deposition within channels can impede diffusion and gas molecule adsorption [9].

The adsorption capacity of cage-type structures at 323 K and 1 bar surpasses that of channel-type structures, attributed to higher gas molecule penetration into the cage structure, enhancing adsorptive capacity. These affirmations align with Qin and co-workers' (2017) suggestion that cage-type structures act as storage containers for polyatomic molecules based on pore size [12].

The relationship between pore size, surface area, and the adsorption capacity of CH₄ and CO₂ in various zeolites is illustrated (Figure 4). Variations in pore size and surface area significantly impact gas adsorption capacity, with faujasite structures (LPM16-X and LPM16-Y) exhibiting superior adsorption capacity compared to channel-type zeolite (LPM17) due to their larger pore and cage sizes mitigating significant pore blockage. Despite the theoretical expectation of higher surface area and pore volume leading to increased adsorption capacity, mordenite LPM17 exhibits relatively high surface area (505 m²/g) and pore volume (0.17 cm³/g) but does not adhere to this pattern, possibly due to the confinement effect of zeolite structures [15]. Additionally, factors such as pore wall aperture and structure, interaction between surface atoms and diffusing molecules, and channel connectivity influence CH₄ and CO₂ adsorption [16,17].

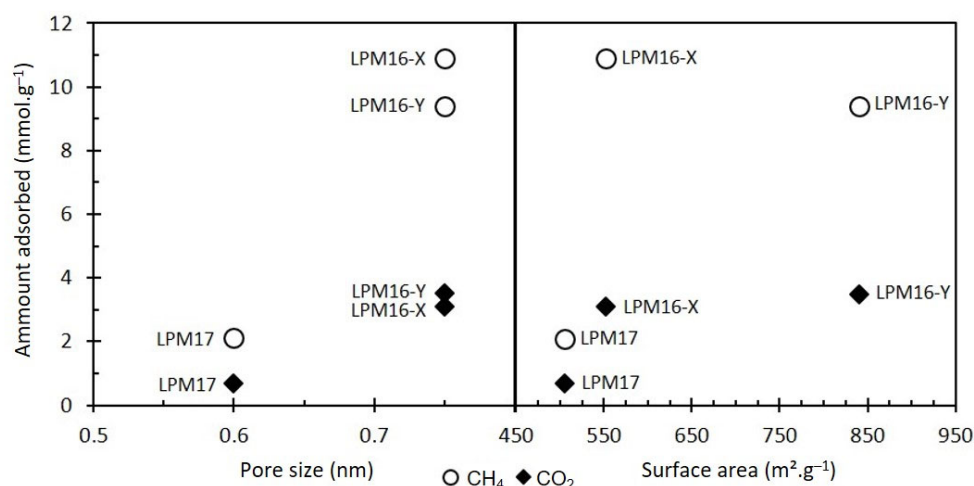


Figure 4. Relationship between pore size, surface area, and adsorption capacity of CH₄ and CO₂.

3.4. Adsorption Isotherms

The adsorption isotherms for CH₄ and CO₂ on cage-type zeolites at 298 K are depicted in Figure 5. The shapes of these curves vary based on the type of adsorbate. Notably, CH₄ exhibits a higher affinity for adsorption compared to CO₂, as indicated by the significant increase in CH₄ adsorption at different pressure levels. Interestingly, CO₂ adsorbs at least ten times less than CH₄, despite their similar kinetic diameters (0.38 nm for CH₄ and 0.33 nm for CO₂), allowing them to pass through the pore openings of zeolites. This difference in affinity between CH₄ and CO₂ in type X and Y zeolites can be attributed to structural charges and cation effects, along with the distinction between cage and channel structures. The polar nature of CO₂ facilitates strong interaction with the negative structural charges balanced by cations in low-SAR zeolites like faujasites. Conversely, nonpolar CH₄ is less favoured in these environments [18,19].

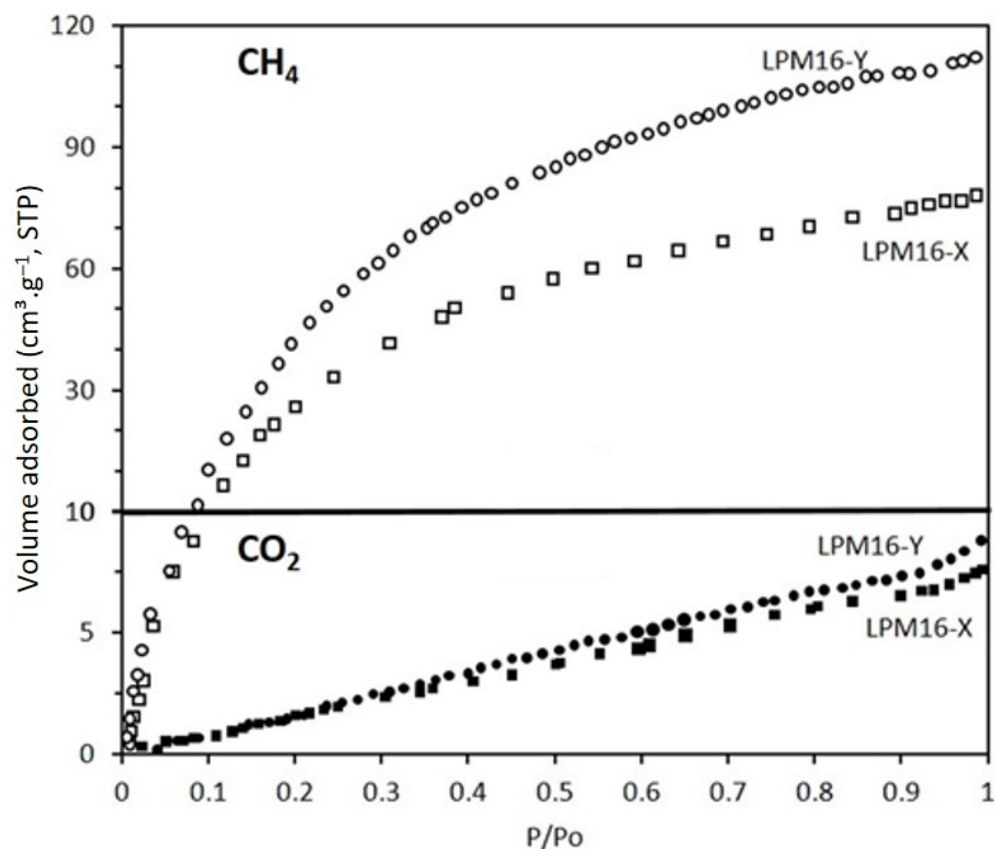


Figure 5. CH₄ and CO₂ adsorption isotherms.

3.5. Adsorption Kinetics

The adsorption dynamics of CH₄ and CO₂ in cage- and channel-type zeolites are illustrated in Supplementary Figure S4, providing valuable insights into their distinct adsorption kinetics. In cage-type zeolites (LPM16-X and LPM16-Y), CH₄ adsorption shows a gradual, nearly linear increase over time, in line with prior research, such as that of Grifone and co-workers (2021), who suggested that CH₄ adsorption primarily results from a confinement effect within the zeolite structure rather than interactions with acidic sites [20]. Conversely, CO₂ adsorption displays convex curves for both zeolite groups. Initially, the adsorption rate is relatively sluggish, followed by a rapid ascent until reaching a plateau, indicating that CO₂ molecules initially bind to robust sites within the zeolite structure, likely influenced by CO₂'s quadrupole moment, before occupying outer structural sites [19]. This disparity in uptake rates between materials LPM16 and LPM17 is partly attributed to the three-dimensional connections between FAU cages, whereas the channels in MOR topology are one-dimensional.

Fractional adsorption curves (q/q_m) were utilised to further elucidate the adsorption characteristics, revealing the influence of the zeolite's structural framework and the properties of the adsorbates. Analysis of initial adsorption rates and equilibrium times, summarised in Supplementary Table S2 and in Figures 6 and 7, offers insights into how molecules interact with zeolites of varying frameworks and physical–chemical properties, critical for understanding the efficiency of the adsorption process.

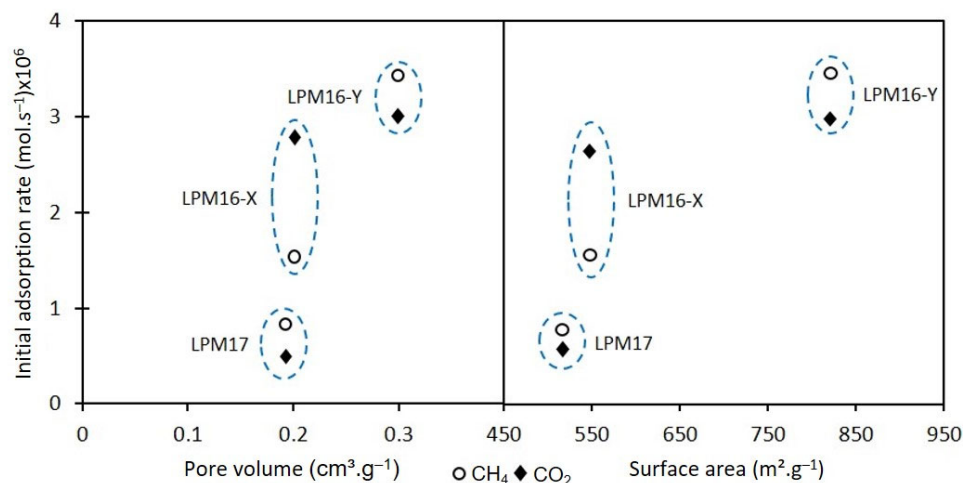


Figure 6. Effects of pore volume and surface area on the initial CH₄ and CO₂ adsorption rate of cage- and channel-type zeolite by-products.

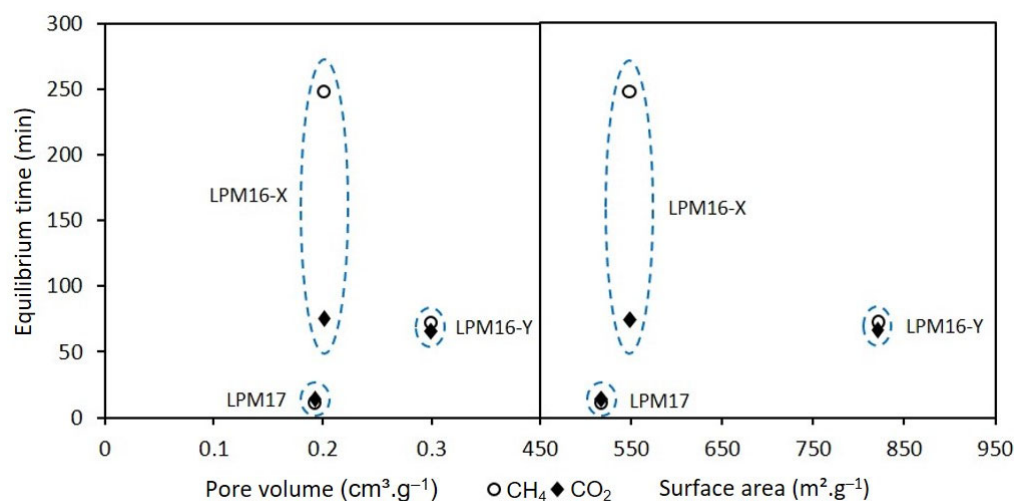


Figure 7. Effects of pore volume and surface area on the CH₄ and CO₂ equilibrium time of cage- and channel-type zeolite by-products.

During the initial adsorption stage (Figure 7), both LPM16-X and LPM16-Y zeolites exhibit higher adsorption rates compared to LPM17 for both gases, suggesting the presence of preferential adsorption sites on the zeolitic surface, potentially including cationic sites and defects within the zeolite structure [21]. Furthermore, the slower adsorption of CH₄ compared to CO₂ may be attributed to differences in molecular structural orientation [19]. While high initial adsorption rates do not necessarily translate to high adsorption capacities, factors such as the size of the adsorbate molecule relative to micropore size and the resistance to diffusion significantly influence the overall adsorption process [16]. Equilibrium time data (Figure 7) reveal that CO₂ reaches equilibrium faster than CH₄, indicating potential interactions between sodium cations and CO₂ molecules. Moreover, zeolites with larger surface areas and pore volumes exhibit longer equilibrium times, possibly due to adsorbates transitioning between adsorption sites before final adsorption occurs [22,23]. The presence of defects in zeolites resulting from the lithium extraction process also plays a crucial role in influencing the adsorption process. Zeolites with larger pore sizes tend to have longer equilibrium times, likely due to the presence of defects within the zeolite structure [4]. In contrast, channel-type zeolites achieve equilibrium in less than 50 min, probably due to the specific pore network system and strong molecule–zeolite interactions within the channels.

3.6. Adsorbate–Adsorbent Interaction

The FT-IR spectra of adsorbed CH₄ molecules, depicted in Supplementary Figure S5 within the regions of 3200–2800 cm^{−1} and 1500–1200 cm^{−1}, emphasise the asymmetric band peaks (3040–2970 cm^{−1}) and symmetrical peaks (1380–1335 cm^{−1}) [24]. During gas adsorption, the interaction between molecules and a solid surface is influenced by experimental conditions (temperature and pressure), gas type, and the surface properties of the adsorbent. In macroporous materials, the dominant interaction is adsorbate–adsorbate, while in microporous materials, adsorbent–adsorbate interaction prevails [25,26]. This interaction is reflected in the asymmetric and symmetric bands visible in the FT-IR spectra due to electrostatic forces such as C–Na, H–O, Si–C, O–Na, O–Si, and C–O between CH₄ and CO₂ molecules and zeolites [11].

The peak observed at approximately 3020 cm^{−1} indicates the asymmetric band of adsorbed CH₄, signifying the free rotation of adsorbed molecules around a single axis perpendicular to the adsorbent's surface [11]. Notably, peak intensities in cage-type zeolites (LPM16-X and LPM16-Y) are more pronounced and distinct than those in channel-type zeolites (LPM17). The presence of supercages within faujasite structures (LPM16-X and LPM16-Y) affords greater freedom for adsorbed molecules to rotate, experiencing a symmetric field formed by the zeolite pore walls [27]. Conversely, the appearance of the symmetric band peak around 1365 cm^{−1} suggests weak adsorbate–adsorbent interaction in channel-type zeolites. In contrast, FT-IR spectra for cage-type zeolites exhibit clearer asymmetric and symmetric band peaks due to the confinement effect, indicating a stronger CH₄–zeolite interaction [12,28].

4. Conclusions

The innovative approach presented here has proven effective in obtaining faujasite and mordenite zeolites while facilitating the recovery of lithium from beta-spodumene in the form of Li₂CO₃. The evaluation of these distinct zeolite structures underscores the superior adsorption capabilities of cage-type structures (LPM16-X and LPM16-Y) compared to a channel-type zeolite (LPM17). It was noted that the presence of structural defects resulting from synthesis enhances the availability of active sites, although the presence of an amorphous phase restricts gas adsorption in LPM17. Thermodynamic data elucidate the influence of adsorbate properties, such as the nonpolar nature of CH₄ and the quadrupole moment of CO₂, on adsorption. In distinguishing between the affinities of CH₄ and CO₂ in type X and Y zeolites (LPM16), structural charges and cationic effects play a more significant role than the distinctions between cage and channel structures. Specifically, the polar nature of CO₂ promotes strong interaction with negatively charged structural sites balanced by cations in low-SAR zeolites. Furthermore, the variation in absorption rates between LPM16 and LPM17 materials can be partly attributed to the three-dimensional connections among FAU cages, while MOR topology channels are one-dimensional.

5. Patents

The invention patent resulting from the work reported in this manuscript was issued under record number BR102018016312-4.

Supplementary Materials: The following supporting information can be downloaded at: <https://www.mdpi.com/article/10.3390/min14050526/s1>, Figure S1: FT-IR spectra of zeolite by-products; Figure S2: SEM images: (a) beta-spodumene; (b) LPM16-X; (c) LPM16-Y; and (d) LPM17; Figure S3: Experimental isotherms for cage- and channel-type zeolites; Figure S4: CH₄ and CO₂ fractional uptake curves of cage- and channel-type zeolites at 323 K and 1 bar; Figure S5: FT-IR spectra of CH₄ adsorbed on cage- and channel-type zeolites at 293 K and 1 bar; Table S1: Structural groups detailed via FT-IR spectroscopy; Table S2: Initial adsorption rate, equilibrium time and adsorption capacity of CH₄ and CO₂ on cage- and channel-type zeolites.

Author Contributions: Conceptualization, L.L.d.S. and S.B.C.P.; methodology, L.L.d.S.; software, L.L.d.S.; validation, L.L.d.S., S.B.C.P. and R.M.d.N.; formal analysis, L.L.d.S. and S.B.C.P.; investigation, L.L.d.S.; resources, S.B.C.P. and R.M.d.N.; data curation, L.L.d.S. and S.B.C.P.; writing—original draft preparation, L.L.d.S.; writing—review and editing, S.B.C.P.; visualization, L.L.d.S. and S.B.C.P.; supervision, S.B.C.P. and R.M.d.N.; project administration, S.B.C.P. and R.M.d.N.; funding acquisition, S.B.C.P. All authors have read and agreed to the published version of the manuscript.

Funding: This research was funded by PROEX/CAPES, financing code 001.

Data Availability Statement: We declare that not all data are available due to privacy or ethical restrictions.

Acknowledgments: The authors acknowledge financial support from the CAPES program, the provision of the beta-spodumene sample by CBL, and all assistance provided by Instituto de Tecnología Química (ITQ/Valencia, Spain) in the material characterisations.

Conflicts of Interest: The authors declare no conflicts of interest.

References

1. Liu, Y.; Ma, B.; Lü, Y.; Wang, C.; Chen, Y. A review of lithium extraction from natural resources. *Int. J. Miner. Metall. Mater.* **2023**, *30*, 209–224. [\[CrossRef\]](#)
2. Ackley, M.W.; Rege, S.U.; Saxena, H. Application of natural zeolites in the purification and separation of gases. *Microporous Mesoporous Mater.* **2003**, *61*, 25–42. [\[CrossRef\]](#)
3. Najafi, A.M.; Soltanali, S.; Ghassabzadeh, H. Enhancing the CO₂, CH₄, and N₂ adsorption and kinetic performance on FAU zeolites for CO₂ capture from flue gas by metal incorporation technique. *Chem. Eng. J.* **2023**, *468*, 143719. [\[CrossRef\]](#)
4. Moradi, H.; Azizpour, H.; Bahmanyar, H.; Rezamandi, N.; Zahedi, P. Effect of Si/Al Ratio in the Faujasite Structure on Adsorption of Methane and Nitrogen: A Molecular Dynamics Study. *Chem. Eng. Technol.* **2021**, *44*, 1221–1226. [\[CrossRef\]](#)
5. Najafi, A.M.; Khorasheh, F.; Soltanali, S.; Ghassabzadeh, H. Equilibrium and Kinetic Insights into the Comprehensive Investigation of CO₂, CH₄, and N₂ Adsorption on Cation-Exchanged X and Y Faujasite Zeolites. *Langmuir* **2023**, *39*, 15535–15546. [\[CrossRef\]](#) [\[PubMed\]](#)
6. Kenvin, J.; Mitchell, S.; Sterling, M.; Warringham, R.; Keller, T.C.; Crivelli, P.; Jagiello, J.; Pérez-Ramírez, J. Quantifying the Complex Pore Architecture of Hierarchical Faujasite Zeolites and the Impact on Diffusion. *Adv. Funct. Mater.* **2016**, *26*, 5621–5630. [\[CrossRef\]](#)
7. Garcia, G.; Cabrera, S.; Hedlund, J.; Mouzon, J. Selective synthesis of FAU-type zeolites. *J. Cryst. Growth* **2018**, *489*, 36–41. [\[CrossRef\]](#)
8. Ferdov, S. Conventional synthesis of layer-like zeolites with faujasite (FAU) structure and their pathway of crystallization. *Microporous Mesoporous Mater.* **2020**, *303*, 110263. [\[CrossRef\]](#)
9. Wolfgang, L. Zeolite Y: Synthesis, Modification, and Properties—A Case Revisited. *Adv. Mater. Sci. Eng.* **2014**, *2014*, 724248. [\[CrossRef\]](#)
10. Cairon, O. Impacts of composition and post-treatment on the Brønsted acidity of steam-treated faujasite: Insights from FTIR spectroscopy. *ChemPhysChem* **2013**, *14*, 244–251. [\[CrossRef\]](#)
11. Cairon, O. CO adsorption on N₂-precovered NaY faujasite: A FTIR analysis of the resulting adsorbed species. *ChemPhysChem* **2013**, *14*, 2744–2749. [\[CrossRef\]](#) [\[PubMed\]](#)
12. Qin, Z.; Cychosz, K.A.; Melinte, G.; El Siblani, H.; Gilson, J.-P.; Thommes, M.; Fernandez, C.; Mintova, S.; Ersen, O.; Valtchev, V. Opening the Cages of Faujasite-Type Zeolite. *J. Am. Chem. Soc.* **2017**, *139*, 17273–17276. [\[CrossRef\]](#)
13. Narayanan, S.; Tamizhdurai, P.; Mangesh, V.L.; Ragupathi, C.; Krishnan, P.S.; Ramesh, A. Recent advances in the synthesis and applications of mordenite zeolite—Review. *RSC Adv.* **2020**, *11*, 250–267. [\[CrossRef\]](#) [\[PubMed\]](#)
14. Jiang, N.; Erdos, M.; Moulton, O.A.; Shang, R.; Vlugt, T.J.H.; Heijman, S.G.J.; Rietveld, L.C. The adsorption mechanisms of organic micropollutants on high-silica zeolites causing S-shaped adsorption isotherms: An experimental and Monte Carlo simulation study. *Chem. Eng. J.* **2020**, *389*, 123968. [\[CrossRef\]](#)
15. Derouane, E.G.; Chang, C.D. Confinement effects in the adsorption of simple bases by zeolites. *Microporous Mesoporous Mater.* **2000**, *35–36*, 425–433. [\[CrossRef\]](#)
16. Jensen, N.K.; Rufford, T.E.; Watson, G.; Zhang, D.K.; Chan, K.I.; May, E.F. Screening Zeolites for Gas Separation Applications Involving Methane, Nitrogen, and Carbon Dioxide. *J. Chem. Eng. Data* **2011**, *57*, 106–113. [\[CrossRef\]](#)
17. Ahn, H.; Moon, J.-H.; Hyun, S.-H.; Lee, C.-H. Diffusion mechanism of carbon dioxide in zeolite 4A and CaX pellets. *Adsorption* **2004**, *10*, 111–128. [\[CrossRef\]](#)
18. Bonenfant, D.; Kharoune, M.; Niquette, P.; Mimeault, M.; Hausler, R. Advances in principal factors influencing carbon dioxide adsorption on zeolites. *Sci. Technol. Adv. Mater.* **2008**, *9*, 013007. [\[CrossRef\]](#) [\[PubMed\]](#)
19. Walton, K.S.; Abney, M.B.; LeVan, M.D. CO₂ adsorption in Y and X zeolites modified by alkali metal cation exchange. *Microporous Mesoporous Mater.* **2006**, *91*, 78–84. [\[CrossRef\]](#)

20. Grifoni, E.; Piccini, G.; Lercher, J.A.; Glezakou, V.-A.; Rousseau, R.; Parrinello, M. Confinement effects and acid strength in zeolites. *Nat. Commun.* **2021**, *12*, 2630. [[CrossRef](#)]
21. Boer, D.G.; Langerak, J.; Pescarmona, P.P. Zeolites as Selective Adsorbents for CO₂ Separation. *ACS Appl. Energy Mater.* **2023**, *6*, 2634–2656. [[CrossRef](#)]
22. Ilić, B.; Wettstein, S.G. A review of adsorbate and temperature-induced zeolite framework flexibility. *Microporous Mesoporous Mater.* **2017**, *239*, 221–234. [[CrossRef](#)]
23. Klimeš, J.; Tew, D.P. Efficient and accurate description of adsorption in zeolites. *J. Chem. Phys.* **2019**, *151*, 234108. [[CrossRef](#)] [[PubMed](#)]
24. Villarreal, A.; Garbarino, G.; Riani, P.; Finocchio, E.; Bosio, B.; Ramírez, J.; Busca, G. Adsorption and separation of CO₂ from N₂-rich gas on zeolites: Na-X faujasite vs. Na-mordenite. *J. CO₂ Util.* **2017**, *19*, 266–275. [[CrossRef](#)]
25. Halasz, I.; Kim, S.; Marcus, B. Hydrophilic and hydrophobic adsorption on Y zeolites. *Mol. Phys.* **2002**, *100*, 3123–3132. [[CrossRef](#)]
26. Pérez-Botella, E.; Valencia, S.; Rey, F. Zeolites in Adsorption Processes: State of the Art and Future Prospects. *Chem. Rev.* **2022**, *122*, 17647–17695. [[CrossRef](#)] [[PubMed](#)]
27. Maurin, G.; Bell, R.; Kuchta, B.; Poyet, T.; Llewellyn, P. Adsorption of non polar and quadrupolar gases in siliceous Faujasite: Molecular simulations and experiments. *Adsorption* **2005**, *11*, 331–336. [[CrossRef](#)]
28. Nor Kamarudin, K.S.; Yuan, C.Y.; Hamdan, H.; Mat, H. Ftir Spectroscopy of Methane Adsorption on Zeolites. *J. Chem. Nat. Resour. Engineering* **2008**, *2*, 31–39.

Disclaimer/Publisher’s Note: The statements, opinions and data contained in all publications are solely those of the individual author(s) and contributor(s) and not of MDPI and/or the editor(s). MDPI and/or the editor(s) disclaim responsibility for any injury to people or property resulting from any ideas, methods, instructions or products referred to in the content.